# Design and control of a self-powered hybrid electromagnetic damper

Maziar Jamshidi [a, b, *], Chih-chen Chang [a], Ali Bakhshi [b]

[a] Department of Civil and Environmental Engineering, Hong Kong University of Science and Technology, Clear Water Bay, Kowloon, Hong Kong
[b] Department of Civil Engineering, Sharif University of Technology, Azadi Ave., Tehran, Iran

## ARTICLE INFO

## ABSTRACT

In this paper, the characteristics of a hybrid regenerative electromagnetic (EM) damper are first determined and experimentally examined. The main idea is to have two modes of operation for the EM damper, namely passive energy harvesting and semi-active modes. In the passive mode, the vibrational energy of an underlying structure is harvested and stored in a rechargeable battery. The harvested energy can then be employed in the semi-active control mode to supply the power demand for the required sensors and microcontroller. This hybrid damper would thus be capable of realizing the characteristics of a self-powered EM damper. A prototype of the damper was designed and tested under different harmonic excitations. The mechanical and electrical characteristics of both passive and semi-active modes were investigated and verified. The average harvested power and current were measured, and the efficiency of the different elements of the damper is determined. Next, for tuning the semi-active mode, a sliding mode control algorithm was proposed which considers the inherent nonlinear parasitic force of the EM damper. The proposed algorithm aims to track the response of an optimally controlled structure, by having knowledge of the bound of the nonlinear parasitic force. Finally, the effects of the proposed damper and sliding mode controller for vibration mitigation of a small-scale structure is demonstrated through a series of shake table tests, under harmonic and random excitations.

© 2018 Elsevier Ltd. All rights reserved.

## 1. Introduction

The physical principle behind electromagnetic (EM) transducers is in converting mechanical into electrical energy and vice versa. Depending on the conversion interface, they can be used as actuators, dampers, sensors, or energy harvesters. When employed in a vibration control system, EM dampers have the advantage of recovering the vibrational energy which needs to be removed from the structure. By applying harvesting techniques, this energy can be harvested and stored in the form of electrical energy. In comparison, most of the other types of dampers, such as viscous, magnetorheological (MR), and frictional dampers, would eventually dissipate the absorbed energy as heat. In the past few decades, there has been a surge of interest in energy harvesting from the vibrational source induced by an environmental disturbance. In civil engineering, these

---

* Corresponding author. Department of Civil and Environmental Engineering, Hong Kong University of Science and Technology, Clear Water Bay, Kowloon, Hong Kong.
E-mail address: mjamshidi@ust.hk (M. Jamshidi).

harvesters can be small-scale oscillators attached to a host structure which have a negligible damping on the underlying structure [1–4], or large-scale regenerative dampers that can accommodate both damping and harvesting features [5,6]. Either employed in a tuned mass damper [7–11] or as a single device [12–15], these harvesters aim to harness the damped energy and to power the sensing and processing units of a structural monitoring and control system. It also seems feasible to engage regenerative dampers with a semi-active control action as their power demand is lower [8,9,11,16].

For an EM damper, no additional power is necessary to generate the damping force and its equivalent damping can be adjusted using a simple switched circuit [8]. However, an MR damper requires an external power supply to the current driver in order to generate the magnetic field. Researchers proposed smart regenerative dampers by attaching an MR damper to an EM harvester [17–19]. In those cases, damping is mainly produced by the MR damper, rather than the EM harvester. Alternatively, incorporation of the damper and harvester in a single EM device could be more efficient. Moreover, using an EM damper has this advantage that the vibrational energy can be recovered outside the machine. This reduces the problem associated with self-heating of the damper [14].

In a typical regenerative semi-active damper, the various devices, like sensors and microcontrollers, drain the harvested energy. Because of the random nature of the harvested power, it is possible that the available energy is less than the operational requirement of the system. Therefore, energy outages are very likely, and could negatively affect the control performance. In Ref. [20], a hybrid EM damper was proposed which separates the passive energy harvesting and semi-active modes. The damper switches from the passive mode to the semi-active mode, once sufficient energy is harvested. This allows a robust realization of the self-powered damper, without compromising the vibration control performance.

There are a number of electrical circuits and configurations that can facilitate the energy harvesting function [21–25]. Each interface circuit exhibits a different electrical impedance, which is linked directly to the constitutive relation of the damper. In particular, Lefeuvre et al. [24] proposed a circuitry based on a buck-boost converter that was able to emulate a constant optimal resistance. This favorable property was utilized by Shen and Zhu [13] for simultaneous energy harvesting and passive damping. However, the operating conditions associated with most of the harvesting circuits make them less flexible to be tuned in a semi-active system [8,11,24]. This could diminish the effectiveness of the semi-active controller by limiting the range of damping coefficients that could be provided. As one of the possible remedies, it was proposed in Ref. [20] to separate the operation of an EM damper into a passive energy harvesting mode and a semi-active control mode. As a result, the semi-active mode could cover a larger area of force-velocity domain, without dealing with the complications of the energy harvesting circuit. Consequently, the performance of the damper in mitigating the vibration could be improved.

In this paper, the physical realization of the damper proposed in Ref. [20] is presented. First, the mechanism of the damper and its potential advantages are described in Section 2. Section 3 elaborates on the prototyping of the damper, and Section 4 presents the experimental test results of the prototype. In Section 5, a semi-active control algorithm is proposed for the case that the damper is utilized to suppress the vibration of a single degree-of-freedom (SDOF) structure under ground motion. In Section 6, two modes of the hybrid damper are experimentally investigated for vibration control of a small-scale shear frame model under base excitation. This section aims to demonstrate the real application of the damper.

## 2. Background

Fig. 1(a) illustrates the schematic diagram of a linear EM motor attached to the proposed hybrid control circuit. According to Faraday's law of induction, the linear velocity of the motor $\dot{x}$ creates a back electromotive force (back-emf) voltage $e$, when the terminals of the coil are left open. When the motor is connected to the circuit, this back-emf causes current $i$ to flow inside the circuit. Based on Lorentz law, a reactive force $f_{em}$ is exerted in the opposite direction to the motion. Mathematically, the electro-mechanical relationship of the motor can be described as,

$$e(t) = k\dot{x}(t) \tag{1}$$

$$f_{em}(t) = ki(t) \tag{2}$$

where $k$ is the linear motor constant. The circuit attached to the coil governs the relationship between $i$ and $e$ and determines the relationship between the velocity and the force generated due to the electromagnetic action. In an ideal case, this force is equal to the total force $f$ exerted by the damper. However, in practice, the total force $f$ comprises an additional term $f_p$, which can be attributed to the presence of parasitic damping and friction,

$$f = f_{em} + f_p \tag{3}$$

For the proposed damper, the circuit demonstrated in Fig. 1(b) is able to realize the hybrid feature. By controlling switch 1 (SW1), the damper's mode of operation can alternate between the passive and semi-active modes. The available energy harvested from the vibration can be employed to choose the mode adjustment.

### 2.1. Passive energy harvesting mode

Once SW1 is connected and SW2 is left open, the damper begins to harvest energy and the EM motor exhibits a constant damping coefficient. As shown in Fig. 1(b), the EM motor is first connected to a diode bridge rectifier, which converts the AC
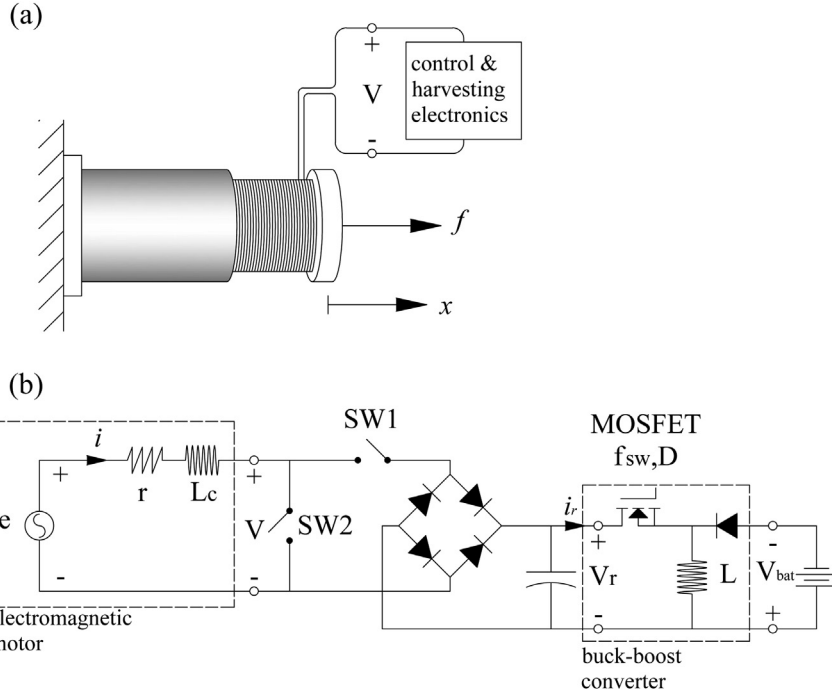
**Fig. 1.** Schematic diagram of (a) a linear EM motor, and (b) the hybrid control circuit.

input voltage induced from the vibration to DC voltage. The DC-DC buck-boost converter then receives this DC output and pumps current into a rechargeable battery. The metal-oxide-semiconductor field-effect transistor (MOSFET) in the circuit is switched on and off by a pulse width modulation (PWM) signal, which is a square wave with a high frequency $f_{sw}$ and a constant duty cycle $D$. Duty cycle is the duration the switch is "on" over the switching period. The equivalent resistance of the circuit $R_0$ can be defined as [24],

$$R_0 = \frac{2Lf_{sw}}{D^2} \tag{4}$$

where $L$ is the inductance of the converter. Eq. (4) is valid as long as the current in the inductor drops back to zero in each switching cycle. This condition occurs when the following discontinuous conduction mode (DCM) criterion is satisfied,

$$V_r < \frac{1-D}{D}V_{bat} \tag{5}$$

where $V_r$ and $V_{bat}$ are the output voltages of the rectifier and the battery, respectively. Assuming that the bridge voltage drop is negligible compared to the input voltage, and, by adding a small ripple capacitor, the dynamics of the coil current can be represented by the following differential equation,

$$e = (r + R_0)\, i + L_c\frac{d\,i}{d\,t} \tag{6}$$

where $r$ and $L_c$ are the coil resistance and inductance, respectively. For low frequency vibration of civil engineering structures, which is usually below 10 Hz, coil inductance ($L_c$) has a very small impedance. Therefore, Eq. (6) can be further simplified as [12],

$$i = \frac{e}{r + R_0} \tag{7}$$

Eqs. (1), (2) and (7) can be used together to find the electromagnetic force-velocity relationship of the damper,

$$f_{em} = \frac{k^2}{r + R_0}\,\dot{x} \tag{8}$$

## 2.2. Semi-active mode

In the semi-active mode, SW1 is disconnected and the harvesting circuit stops storing the current in the battery. In this mode, a PWM signal with a fixed frequency $F_{sw}$ and a variable duty cycle $d$, feeds into SW2. This signal periodically cuts off the current flowing through the coil. With a switching frequency higher than the frequency of the input vibration, the back-emf $e$ can be considered constant during each switching period. In this case, the average current determines the electromagnetic force of the damper and the effect of higher frequencies can be ignored. However, the impedance of the coil inductance cannot be ignored under high frequency PWM. As the time constant of the coil ($\tau = L_c/r$) determines the duration taken for the current to pass through the transient state, it is possible that the switch could turn off before the current reaches its steady state. To avoid that condition, it is suggested that the duration of SW2 "on" be at least four times larger than the time constant of the circuit. The limit for the maximum frequency of SW2 can therefore be set as,

$$F_{sw} < \frac{r}{4L_c}d \qquad (9)$$

Under this condition, the current and voltage waveform of the coil are as shown in Fig. 2. The equivalent average resistance of the circuit during each switching cycle is calculated as,

$$R_{eq} = \frac{r}{d} \qquad (10)$$

Also, the equivalent electromagnetic damping coefficient of the circuit is,

$$c_{em,eq} = \frac{k^2}{r}d \qquad (11)$$

Since the damping is proportional to the duty cycle, for a range of duty cycles between $d_{min}$ to $d_{max}$, the range for the electromagnetic damping can be adjusted as,

$$\frac{k^2}{r}d_{min} \leq c_{em,eq} \leq \frac{k^2}{r}d_{max} \qquad (12)$$

Note that, unlike the damping coefficient in the passive case that is restricted by the DCM condition (Eq. (5)), the damping coefficient in the semi-active case is not limited by an underlying condition. This makes it possible for the damper to have a larger range of damping coefficients, without the restriction associated with the energy harvesting circuit. This is the main reason for decoupling the passive mode from the semi-active mode using switch SW1 in the current design.

The variable damping coefficient can be determined from a semi-active control algorithm, which receives the sensor measurements from the structure and calculates the desired damping coefficient. Additional discussion on the control algorithm is provided in Section 5. The microcontroller calculates and generates the command signal to the switch. During this process, the power needed to supply the monitoring units and processors can be provided by the harvested energy stored in the rechargeable battery during the passive mode.

## 3. Prototyping

The EM motor used for the experiment is a linear voice coil motor with a coil length of 50.8 mm and a diameter of 44.5 mm [26]. The measured coil resistance is 6.8 Ω, and the coil inductance is 4 mH. The linear motor constant is measured to be 23 N/A.
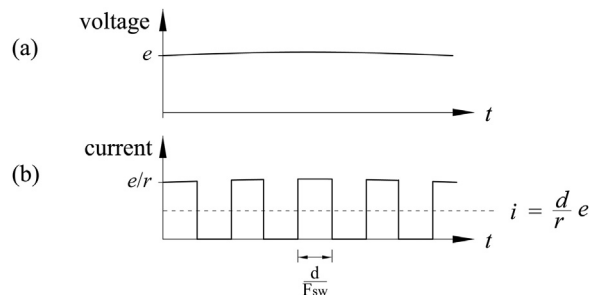


Fig. 2. (a) Voltage, and (b) current waveforms of coil during the switching of SW2.

The schematic of the passive circuit and its prototype adopted in this study are depicted in Fig. 3. For the buck-boost converter, three 220-μH inductors are connected in parallel resulting in 73.33 μH equivalent inductance. MOSFET switch M1 was triggered by the PWM signal from a crystal oscillator (OV-7604-C7, Micro Crystal). The frequency of the signal was 32.768 kHz with a 50% duty cycle and the amplitude was 5 V. An n-channel power MOSFET (FQPF20N06) with 2 V gate threshold was chosen for this application. A smoothing capacitor C1 of capacitance 100 μF was used to reduce the ripple of the output voltage from the rectifier. A pack of 4 NiMH battery cells with 1.2 V nominal voltage per cell was used as the storage unit. Capacitor C2 with the capacitance of 100 μF was added to filter any ripple current that might occur across the battery [24]. A Schottky diode D5 with a low forward voltage drop of 0.39 V was chosen due to its lower current leakage. Four Schottky diodes (D1-D4) are also used to form a full-bridge rectifier with a total forward voltage drop of 0.8 V. The oscillator was supplied by a 4.8 V NiMH battery, and connected to the gate by a 500 Ω R2 resistor. Its current consumption when it is connected to the MOSFET gate was 2.2 mA.

The schematic diagram and a prototype for the semi-active mode are demonstrated in Fig. 4. In order to realize switch SW2 in Fig. 1, two n-channel MOSFETs, M2 and M3 (FQPF20N06), are connected in series with both source terminals connected to each other. This arrangement prevents the blockage of the alternating current by the internal diode of each single MOSFET. The gates of the MOSFETs are triggered by a square wave generated by the controller circuit. The gate voltage $V_G$, shown in Fig. 5(b), alternates between two high and low states $+V_{DC} = +4.5$ V and $-V_{DC} = -4.5$ V. For the positive polarity of $e$, the diode of M3 is forward biased, thus, only M2 does the switching. For this case, since the source terminal of M2 is grounded, the gate-to-source voltage ($V_{G-S}$) is identical to $V_G$. When $e$ changes to negative, M2 is forward biased and M3 operates. Since the source terminal of M3 is not connected to the common ground, the gate-to-source voltage of M3 is floating. As shown in Fig. 5(c), for the amplitude of the back-emf, $e_0$, the floating low state voltage increases up to $e_0-V_{DC}$. To ensure that switching occurs
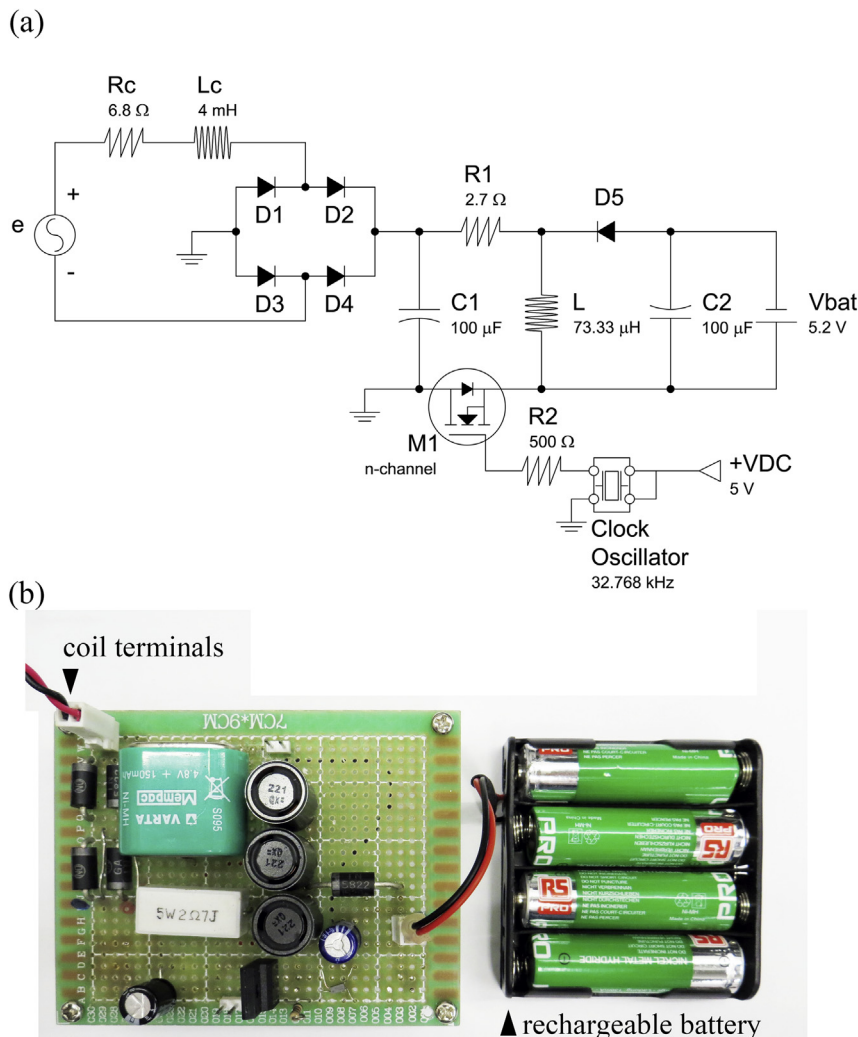


**Fig. 3.** Passive energy harvesting circuit; (a) schematic diagram, and (b) actual prototype.
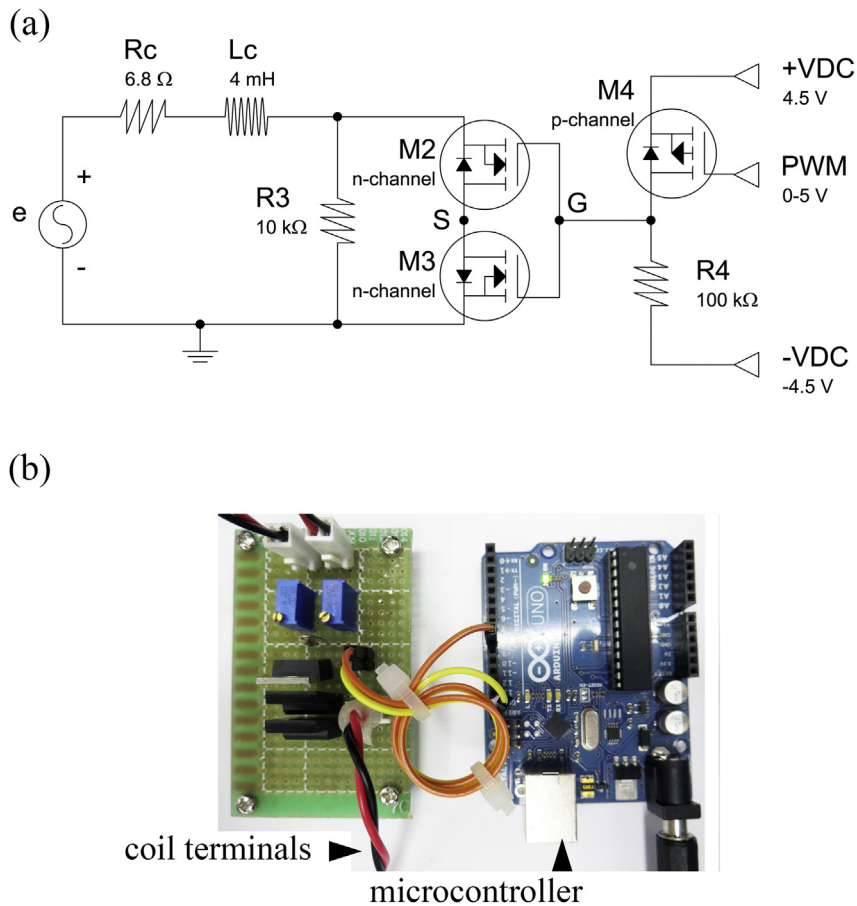
(a)



(b)



**Fig. 4.** Semi-active circuit; (a) schematic diagram, and (b) actual prototype.

properly, $e$ should not be lower than $-6.5\,V$ for a gate threshold voltage of $V_{GS(th)} = 2\,V$, otherwise the low state may not correspond to the "off" state of the switch.

The microcontroller board selected to generate the command signal is Arduino Uno [27], and is capable of producing an output voltage ranging between 0 and 5 V. However, as explained above, $V_G$ should have a negative low state. To achieve that condition, a p-channel MOSFET M4 (FQPF27P06) is connected to a positive and a negative DC supplies, through a current limiting resistor. With this configuration, for a signal with the frequency of $F_{sw}$ and duty cycle of $d'$, coming from the Arduino board, the resulting command signal $V_G$ has the duty cycle of $d = 1- d'$, and the same frequency $F_{sw}$. Resistor R4 with a high resistance of 100 kΩ limits the current (90 μA), and thus the power drawn from the DC voltage supply. When the switch is turned off, the sudden change of current induces a voltage spike across the MOSFETs. To eliminate potential damage, resistor R3 = 10 kΩ is added in parallel to provide a path for the inductor to discharge, and it has a high resistance so that it does not affect the circuit. It should be mentioned that the passive and semi-active circuits can be easily incorporated into a single circuit. However, they have been presented and studied separately for a better elaboration of each mode.

## 4. Experimental characterization

Fig. 6 shows the experimental set-up for testing the prototype of the damper. To generate the harmonic excitation, a single-axis shake table was utilized. The displacement and force of the damper were measured via a load cell and a laser displacement sensor. As mentioned earlier, when the terminals of the EM motor are left open and no current flows through the coil, the damping generated from electromagnetic effect is zero. However, the EM motor still produces some additional force due to the inherent parasitic damping and friction force of the device itself. There have been various nonlinear models attempting to describe the mechanical characteristics of this parasitic force depending on the given configuration and design of the EM damper [12,14,28,29]. Similarly, in this study, a rheological model is adopted that includes the parasitic force and assumes a coulomb frictional element in series with a viscous damper, as shown in Fig. 7. The parasitic force can be described as,
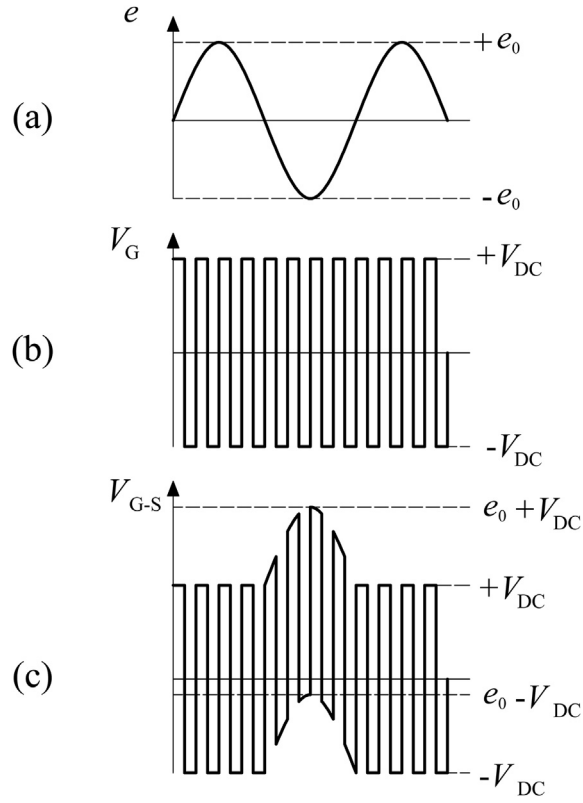
**Fig. 5.** (a) Input back-emf, (b) gate voltage ($V_G$), and (c) gate to source voltage ($V_{G-S}$) waveforms.


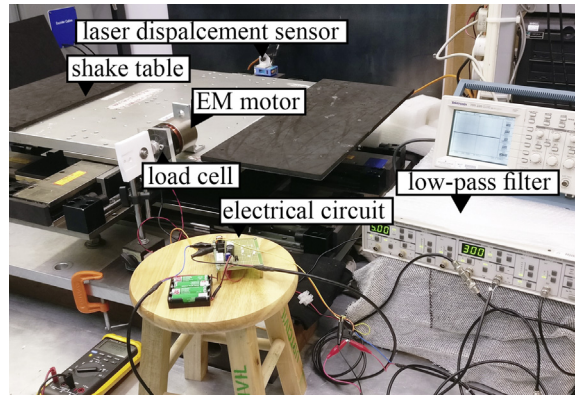
**Fig. 6.** Set-up of the prototype tested using shake table.

$$f_p = \begin{cases} c_p \dot{x}, & c_p|\dot{x}| < f_c \\ f_c \text{sgn}(\dot{x}), & c_p|\dot{x}| > f_c \end{cases} \tag{13}$$

where $c_p$ and $f_c$ are the parasitic viscous damping and friction force of the EM motor.

To find the parasitic parameters defined in Eq. (13), the terminals of the coil were opened. Fig. 8(a) shows the force-velocity diagram of the open-circuit case under the shake table harmonic displacement of 5 mm and frequency of 4 Hz. By applying the Levenberg-Marquardt curve fitting technique [30] to the measured data, $c_p$ and $f_c$ were found. The results of regression under 4, 6, and 8 Hz excitation are summarized in Table 1. The average values are $c_p = 17.79$ N s/m and $f_c = 2.47$ N, respectively. In contrast to the open circuit case where the electromagnetic damping is zero, the damper theoretically has the largest damping $c_{em,short} = k^2/r$ when the terminals of the coil are short-circuited. The force velocity diagram for the short-circuit case
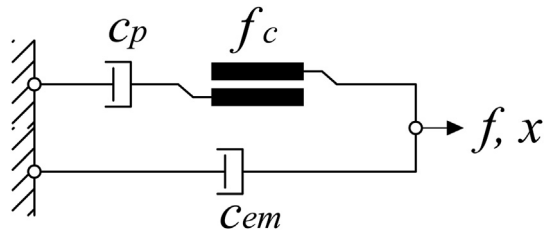
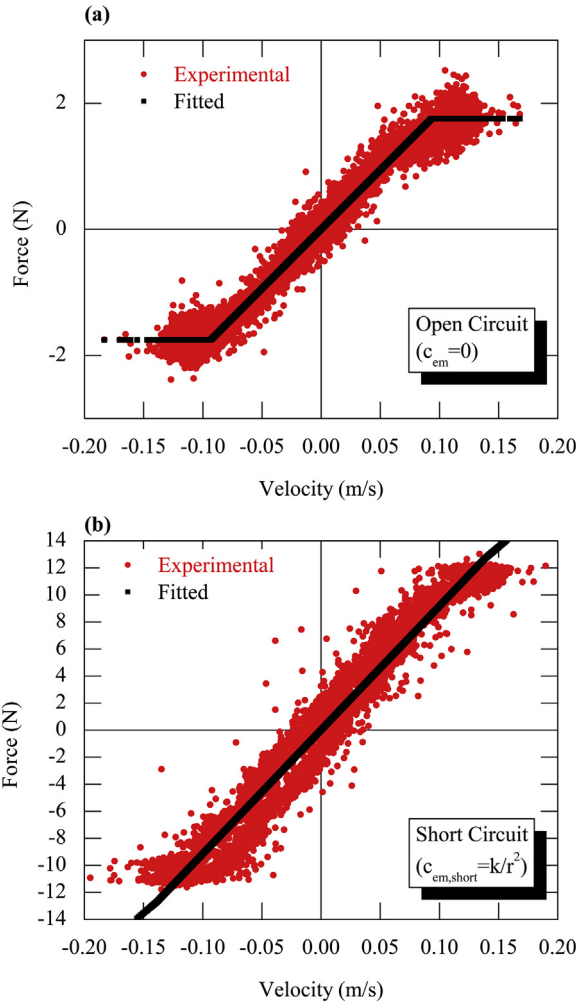**Fig. 7.** Rheological model of the linear EM motor.



**Fig. 8.** Force-velocity relationship of the EM damper; (a) open-circuit, (b) short-circuit [5 mm, 4 Hz].

is plotted in Fig. 8(b). Based on the parasitic properties obtained in the open-circuit case, the added EM damping coefficient can be found again through regression. The average maximum electromagnetic damping under different frequencies is 74.44 N s/m, which is close to the theoretical value of 77.79 N s/m.

## 4.1. Passive energy harvesting mode

To find the emulated average resistance of the buck-boost converter, the input current $i_r$ (see Fig. 1) is calculated by measuring the voltage drop across a small resistor (R1 = 2.7 Ω). This signal was filtered through a low-pass analog filter with a cut-off frequency of 300 Hz. In Fig. 9, the output voltage of the rectifier $V_r$ is plotted versus the filtered current $i_r$ under the excitation frequency of 4 Hz. Linear curve fitting was used to calculate the equivalent resistances, and the values are presented

**Table 1**
Open and short circuit mechanical properties of the EM damper.

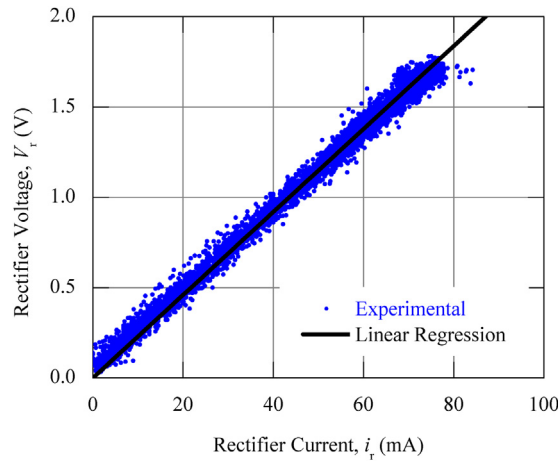| Input excitation | Parasitic damping coefficient, $c_p$ (N s/m) | Friction force, $f_c$ (N) | Short circuit damping coefficient $c_{em,short}$ (N s/m) |
|---|---|---|---|
| d = 5 mm; f = 4 Hz | 19.12 | 1.92 | 73.66 |
| d = 5 mm; f = 6 Hz | 17.89 | 2.51 | 74.91 |
| d = 5 mm; f = 8 Hz | 16.37 | 2.99 | 74.76 |
| **Average** | **17.79** | **2.47** | **74.44** |



**Fig. 9.** Rectifier output voltage ($V_r$) versus current ($i_r$) [5 mm, 4 Hz].

in Table 2 for the excitation frequencies of 4, 6, and 8 Hz. The average resistance of the circuit is 22.5 Ω, which is close to the equivalent value of 19.2 Ω calculated based on Eq. (4).

In Fig. 10, the open-circuit back-emf $e$ is plotted against the current passing through the coil $i$ for vibration frequencies of 4 and 8 Hz. In the range of −0.8 V to 0.8 V, no current passes through the coil, as the result of the bridge voltage drop. Beyond this range, voltage and current exhibit a linear relationship. As can be seen, even though the zero-current zone increases the total equivalent resistance of the circuit, its effect becomes less pronounced as the vibration frequency increases. Hence, for the considered range of frequency, the assumptions made for Eq. (7) are valid and the passive energy harvesting circuit plus the coil show a near constant resistive behavior. The equivalent resistance $R_{passive}$ of the circuit for the different frequencies are given in Table 2 with an average value of 32.4 Ω. The force-velocity diagram of the damper under 4 Hz excitation frequency is also plotted in Fig. 11.

To estimate the amount of harvested power, the average battery current $i_{bat}$ is measured using a high accuracy multimeter. For 4, 6, and 8 Hz of excitation frequencies, the average harvested current flowing into the battery was measured to be 10, 21, and 32 mA, respectively. For the battery voltage of 5.13 V, they correspond to 52, 109, and 166 mW of harvested power. The total efficiency of damper can be defined as,

$$\eta = \frac{\overline{P}_{bat}}{\overline{P}_{in}} \tag{14}$$

where the average mechanical input power to the damper ($\overline{P}_{in}$), and the harvested power to the battery ($\overline{P}_{bat}$) are,

$$\overline{P}_{in} = \frac{1}{t}\int_0^t f.\dot{x}\mathrm{d}\tau \tag{15}$$

**Table 2**
Electrical and mechanical properties of the passive mode circuit.

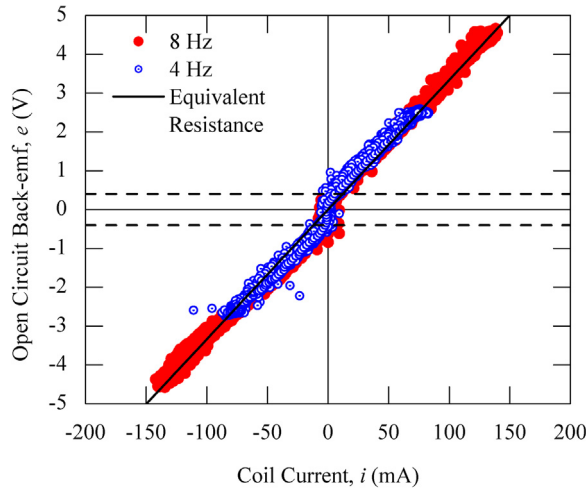| Input excitation | Emulated resistance of the buck-boost converter, $R_0$ (Ω) | Equivalent resistance of the coil and circuit, $R_{passive}$ (Ω) | Equivalent EM damping coefficient $c_{em}$ (N s/m) |
|---|---|---|---|
| d = 5 mm; f = 4 Hz | 23.0 | 33.2 | 15.9 |
| d = 5 mm; f = 6 Hz | 22.4 | 32.0 | 16.5 |
| d = 5 mm; f = 8 Hz | 22.1 | 32.2 | 16.4 |
| **Average** | **22.5** | **32.4** | **16.3** |

**Fig. 10.** Relationship between the induced back-emf and coil current.

$$\overline{P}_{bat} = \frac{1}{t} \int_0^t V_{bat} \cdot i_{bat} d\tau \tag{16}$$

In Table 3, column (8) gives the efficiency of the damper for the three frequencies with an average efficiency factor of 0.29. The main sources of power loss in the damper are the mechanical power loss due to the parasitic force and the electrical power loss inside the coil, diodes conduction loss in the rectifier, and the buck-boost converter components. To investigate the share of each source in the total efficiency, two intermediate efficiencies are defined as below,

$$\eta_1 = \frac{\overline{P}_{em}}{\overline{P}_{in}} \tag{17}$$

$$\eta_2 = \frac{\overline{P}_{bat}}{\overline{P}_{em}} \tag{18}$$
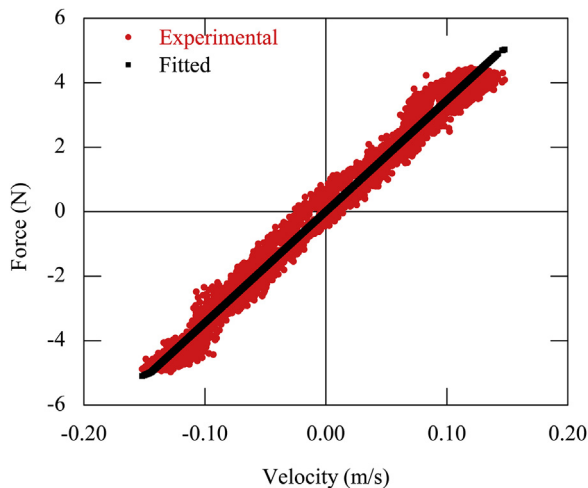
where,



**Fig. 11.** Force-velocity relationship of the damper in the passive energy harvesting mode [5 mm, 4 Hz].

**Table 3**
Harvested power and efficiency.

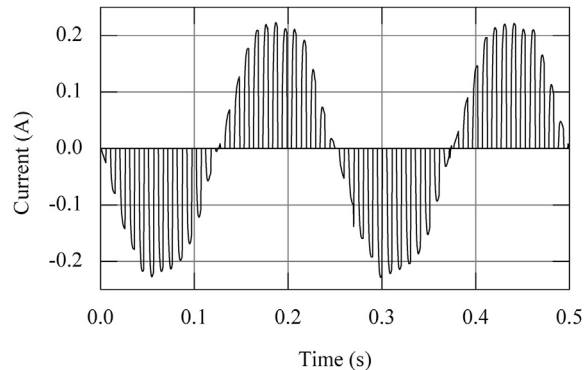| (1) | (2) | (3) | (4) | (5) | (6) | (7) | (8) |
|-----|-----|-----|-----|-----|-----|-----|-----|
| Excitation frequency (Hz) | Battery average current, $i_{bat}$ (mA) | Battery harvested power, $P_{bat}$ (mW) | Input electrical power, $P_{em}$ (mW) | Input mechanical power, $P_{in}$ (mW) | Efficiency $\eta_1$ | Efficiency $\eta_2$ | Efficiency $\eta$ |
| 4 | 10 | 52 | 103 | 217 | 0.47 | 0.50 | 0.24 |
| 6 | 21 | 109 | 208 | 368 | 0.57 | 0.52 | 0.30 |
| 8 | 32 | 166 | 302 | 499 | 0.61 | 0.55 | 0.33 |
| **Average** | – | – | – | – | **0.55** | **0.53** | **0.29** |



**Fig. 12.** Time history of current in the semi-active mode for $d = 0.55$.

$$\overline{P}_{em} = \frac{1}{t} \int_{0}^{t} e \cdot i \mathrm{d}\tau \qquad (19)$$

Efficiency factor $\eta_1$ reflects the contribution of the mechanical power loss, and $\eta_2$ shows the share of the electrical power loss. The average mechanical efficiency $\eta_1$, for the tested prototype, is 0.55, and the average value for the electrical efficiency $\eta_2$ is 0.53. A higher electrical efficiency ($\eta_2$) could be achieved by reducing the equivalent resistant of the buck-boost converter down to the resistance of the coil [31], or by reducing the resistive loss inside the components.

### 4.2. Semi-active mode

Taking a minimum duty cycle of $d_{min} = 0.2$, the switching frequency $F_{sw}$ is set to 100 Hz to satisfy the criterion in Eq. (9). Fig. 12 displays the time history of the current passing through the coil for $d = 0.55$, when the damper is excited with a 5-mm amplitude and 4-Hz harmonic vibration. It can be seen that modulation of the current, and accordingly the force, is done properly. For duty cycle values of 0.15, 0.35, 0.55, and 0.75, the average current, filtered with an analog low-pass filter, is plotted in Fig. 13. The theoretical values are calculated based on Eq. (10) and the open-circuit voltage measurement. It can be seen that the experimental current measurements match quite well with the corresponding theoretical values. As shown in Fig. 14, the semi-active circuit is capable of producing the required resistance by adjusting the duty cycle from $d_{min} = 0.2$ to $d_{max} = 0.8$. This implies that the damper is capable of providing variable damping coefficients between $c_{em,min} = 15.56$ N s/m and $c_{em,max} = 62.23$ N s/m (Eq. (12)) effectively. In Fig. 15, force-velocity relationship of the damper is plotted, when the duty cycle is varied from 0.2 to 0.8. The hatched area in the figure defines the feasible force region of the damper. The boundaries are defined based on the short circuit damping coefficient and the intrinsic parasitic damping coefficient and friction force of the damper. The fact that during the semi-active mode the energy harvesting circuit is disconnected makes it possible to cover a larger area of the force-velocity domain [20].

Finally, to have an estimate of the power consumption of the semi-active mode, the current drawn by the Arduino board connected to two accelerometers (MPU-6050) was measured. It was found that a current of 70–80 mA passed through the board under a 5.2-V DC power supply, which corresponded to power consumption of 364–416 mW. According to the results in Table 3, for the harmonic excitation of 8 Hz and 5 mm, the harvested power of the passive mode is 166 mW. Therefore, by operating in the passive energy harvesting mode for 2–3 min, the damper should be able to sustain the semi-active mode for 1 min.
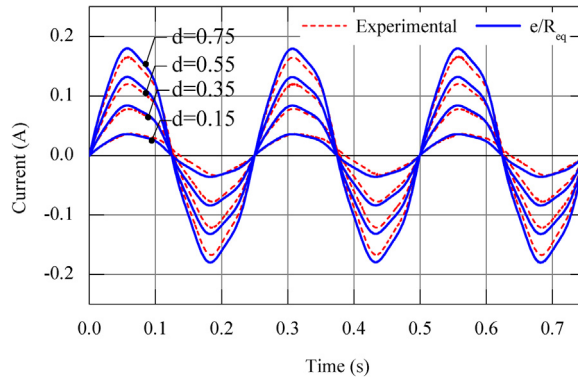
**Fig. 13.** Filtered current for various duty cycles in the semi-active mode ($d = 0.15, 0.35, 0.55, 0.75$).
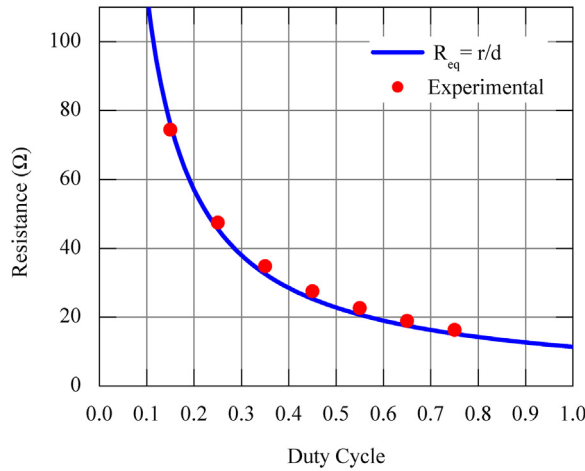


**Fig. 14.** Semi-active circuit equivalent resistance versus duty cycle.
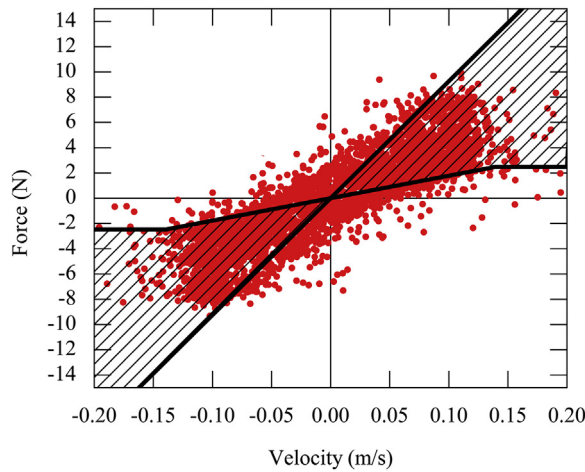


**Fig. 15.** Force-velocity relationship of the damper in the semi-active mode ($d = 0.2$–$0.8$).

## 5. Sliding mode based controller for semi-active mode

As mentioned earlier, the total force exerted on the structure comprises an electromagnetic force $f_{em}$, which can be tuned by the circuit, and a nonlinear parasitic force $f_p$ which depends on the damper's mechanism and properties. Tuning the semi-

active mode, without considering the nonlinear effect of $f_p$ could compromise the performance of the damper. Even though some attempts can be done to find the constitutive model of the parasitic force, finding a general solution that fits all EM devices seems intractable.

In this section, a semi-active control algorithm is adopted to mitigate the vibration of a structure under ground acceleration. The formulations are set-up for a single degree-of-freedom (SDOF) structure, which can easily be extended to multi-degree-of-freedom (MDOF) structures as well. Consider the SDOF model shown in Fig. 16(a), which is equipped with an EM damper. The governing equation of motion can be represented in state-space format as below,

$$\dot{\mathbf{z}} = \mathbf{A}\mathbf{z} + \mathbf{B}\left(f_{em} + f_p\right) + \mathbf{E}\ddot{x}_g \tag{20}$$

where in the state vector $\mathbf{z} = [x, \dot{x}]$, $x$ and $\dot{x}$ are the relative displacement and velocity with respect to the ground, and $\ddot{x}_g$ is the ground acceleration. Force $f_p$ can be considered as a general non-linear term depending on the state $\mathbf{z}$. The problem is to find a robust control force $f_{em}$ that can drive the response of the structure to zero, in the presence of an unknown bounded nonlinear mismatch $f_p$. The sliding mode control technique is a viable method that can resolve this type of problem. Following the procedure proposed in Ref. [32], a sliding mode controller (SMC) was developed to track the response of a closed-loop optimal system. One advantage of the SMC is that it does not require a force feedback loop [33] which can simplify the semi-active control implementation.

Assuming that the EM damper is replaced by an ideal actuator (see Fig. 16(b)), the dynamics of this reference structure can be described as,

$$\dot{\mathbf{z}}_r = \mathbf{A}\mathbf{z}_r + \mathbf{B}u + \mathbf{E}\ddot{x}_g \tag{21}$$

where $\mathbf{z}_{r} = [x_r, \dot{x}_r]$ is the state vector of the reference structure, and $u$ is the input force of an ideal feedback optimal control law, which can be written as,

$$u = \mathbf{G}\mathbf{z}_r \tag{22}$$

Defining an error variable $e$,

$$e = x - x_r \tag{23}$$

The error vector between the actual and the reference structures can be defined as,

$$\mathbf{e} = \left[ e, \quad \dot{e}, \quad \int edt \right]^{\mathrm{T}} \tag{24}$$

Based on Eqs. (20), (21) and (24), the error dynamics takes the following form,
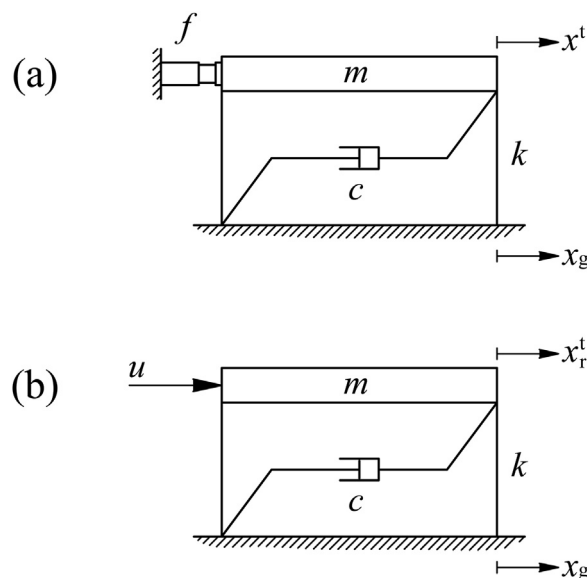


**Fig. 16.** (a) Actual and (b) reference structures.

$$\dot{\mathbf{e}} = \begin{bmatrix} \mathbf{A} + \mathbf{BG} & \mathbf{0}_{2\times 1} \\ 1 & \mathbf{0}_{1\times 2} \end{bmatrix} \mathbf{e} + \begin{bmatrix} -\mathbf{BG} \\ 0 \end{bmatrix} \mathbf{z} + \begin{bmatrix} \mathbf{B} \\ 0 \end{bmatrix} \left( f_{em} + f_p \right) \tag{25}$$

Define a sliding surface or switching function as,

$$\sigma = h_1 e + \dot{e} + h_2 \int e dt = \mathbf{he} \tag{26}$$

where $\mathbf{h}$ is a vector of the weighting factors. According to the sliding mode theorem, for a candidate Lyapunov function $V(\sigma) = \frac{\sigma^2}{2}$, the input $f_{\mathrm{em}}$ is able to drive the variable $\sigma$ to zero in finite time, if $\dot{V}(\sigma) = \sigma\dot{\sigma} \leq 0$. This condition can alternatively be written as [34],

$$\sigma\dot{\sigma} \leq -\beta|\sigma|, \quad \beta > 0 \tag{27}$$

where $\beta$ is a strictly positive constant. By selecting a control input as,

$$\overline{f}_{\mathrm{em}} = m\mathbf{h}\mathbf{A}_e\mathbf{e} + \mathbf{Gz} + \rho\mathrm{sgn}(\sigma), \quad \rho > 0 \tag{28}$$

$$\mathbf{A}_e = \begin{bmatrix} \mathbf{A} + \mathbf{BG} & \mathbf{0}_{2\times 1} \\ 1 & \mathbf{0}_{1\times 2} \end{bmatrix} \tag{29}$$

the derivative of the sliding surface is,

$$\dot{\sigma} = -\frac{1}{m} \left( f_p + \rho\mathrm{sgn}(\sigma) \right) \tag{30}$$

Substituting Eqs. (26) and (30) into Eq. (27), the sliding condition becomes,

$$\rho \geq m\beta - f_p\mathrm{sgn}(\sigma) \tag{31}$$

Thus, the lower bound for parameter $\rho$ in the control force can be determined as,

$$\rho \geq m\beta + |f_p| \tag{32}$$

This equation suggests that knowledge of the bound of nonlinear force $f_p$ is sufficient to ensure that the control force $f_{\mathrm{em}}$ can track the states of the reference structure. It should be noted that the passivity constraint of the semi-active damper is not incorporated in Eq. (32). This passivity constraint prescribes that the damper force must always stay in the dissipative region. By adding that, the actual force takes the following form,

$$f_{\mathrm{em}} = \begin{cases} \overline{f}_{\mathrm{em}}, & \overline{f}_{\mathrm{em}}\dot{x} \geq 0 \\ 0, & \overline{f}_{\mathrm{em}}\dot{x} < 0 \end{cases} \tag{33}$$

Note that when $f_{\mathrm{em}} = 0$, the error trajectory could go off the sliding surface even if Eq. (32) is satisfied. However, the nature of semi-active control guarantees that the closed-loop system always remains stable. After calculating the control force from Eq. (33), the duty cycle $d$ that realizes the damping coefficient of the semi-active mode can be obtained as,

$$d(t) = \frac{r}{k^2} \cdot \frac{f_{\mathrm{em}}(t)}{\dot{x}(t)} \tag{34}$$

## 6. Vibration control of a SDOF model

### 6.1. Experimental set-up

In this section, the performance of the damper is experimentally investigated for vibration mitigation of a single-story small-scale shear frame model under base excitation. The set-up of the experiment is shown in Fig. 17. The aluminum columns are fixed to the shake table. The model can only vibrate in a single lateral axis owing to its relative rigidity in the perpendicular direction. The frame height and span are 34 cm and 26.5 cm, respectively. The effective mass of the model is 2.04 kg and its lateral stiffness is $k_s = 2389$ N/m. An additional 5-kg mass is added to the model, which reduces the natural frequency of the oscillating system to 2.93 Hz. The damping ratio of the original model is around 1%.
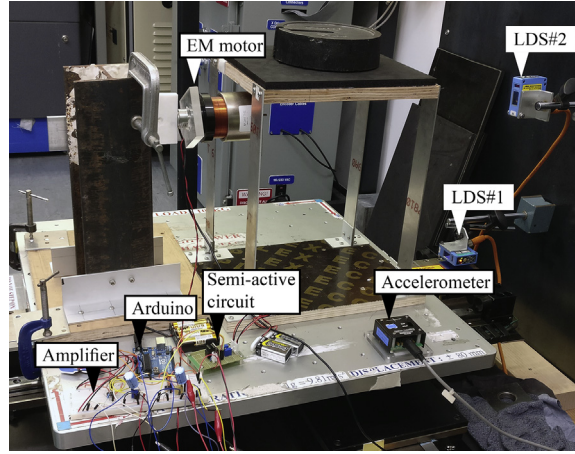
**Fig. 17.** Experimental set-up (semi-active mode).

### 6.2. Passive energy harvesting mode

For the first case, the terminals of the damper are connected to the passive energy harvesting circuit developed in Section 3 (Fig. 3). To evaluate the control performance of the passive circuit, the transmissibility ratio of the model is plotted in Fig. 19 for different excitation frequencies. The data obtained from the experimental measurements are shown with scattered symbols, and the continuous lines show the theoretical graphs. The open-circuit case is included to illustrate the damping effect introduced by the parasitic force alone. Clearly, the uncontrolled model with no damper has the largest transmissibility values. For the passive case, the model resembles the performance of a system with an equivalent damping ratio of $\xi_{\text{passive}} = 12.5\%$, while for the open-circuit case the damping ratio of the system ($\xi_{\text{open}}$) is around 6.5%. The additional 6% damping between the passive and the open-circuit cases is attributed to the electromagnetic damping produced by the circuit. This value is in accordance with the average electromagnetic damping coefficient of 16.3 N s/m (Table 2), which results in a 6.3% added damping to the model.

Regarding the design of the passive energy harvesting mode, there are two main factors that govern the operational range of the harvesting circuit. The back-emf voltage generated by the EM motor must be within a given range in order to exhibit a constant resistance and hence a constant damping coefficient. The lower bound of the voltage is determined by the voltage drop across the bridge rectifier. When the input back-emf $e$ is smaller than the bridge voltage drop $V_d$, no current passes through the circuit, no electromagnetic damping is produced, and no energy is harvested. The effect of voltage drop becomes insignificant as the amplitude of the back-emf $e_0$ increases. The back-emf amplitude is related to the relative velocity of the model with respect to the ground. For a linear SDOF system under ground excitation, the transfer function relating the velocity of the structure to the ground displacement is,

$$R_v(\omega; \omega_n, \xi) = \frac{\dot{x}_0}{x_{g,0}} = \omega \cdot \frac{(\omega/\omega_n)^2}{\left[\left(1 - (\omega/\omega_n)^2\right)^2 + (2\xi\omega/\omega_n)^2\right]^{\frac{1}{2}}} \tag{35}$$

where $x_{g,0}$ and $\omega$ are the base displacement and frequency respectively, $\omega_n$ is the model natural frequency, and $\xi$ is the model equivalent damping ratio. Therefore, the amplitude of open-circuit back-emf voltage can be found as,

$$e_0^{\text{open}} = kx_{g,0}R_v(\omega; \omega_n, \xi_{\text{open}}) \tag{36}$$

where $\xi_{\text{open}}$ is the model equivalent damping ratio for the open-circuit case. Fig. 20(a) shows the variation of open-circuit voltage amplitude for the given experimental model. For a voltage drop of $V_d = 0.8$ V, the white area shows the region that $e_0^{\text{open}} < 0.8$ V. Beyond that region, the passive energy harvesting circuit begins to produce damping and harvest energy.

On the other hand, the upper bound of voltage is determined by the DCM condition given in Eq. (5). The rectifier voltage $V_r$ under DCM condition can be estimated as,

$$V_{r,0} = \left(e_0^{\text{passive}} - V_d\right) \cdot \frac{R_0}{R_0 + r} \tag{37}$$

where the back-emf amplitude of the passive case is

## (a) Passive energy harvesting mode
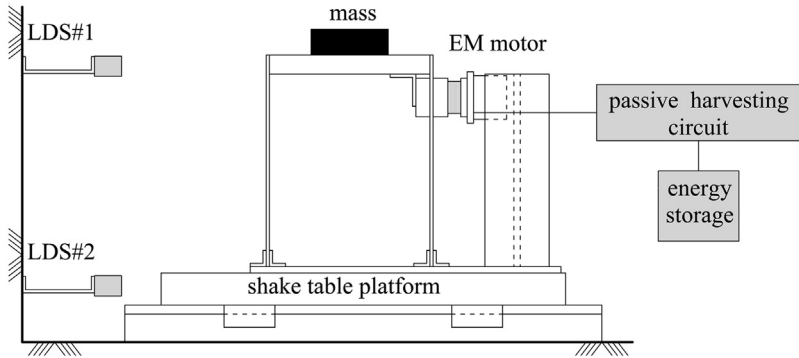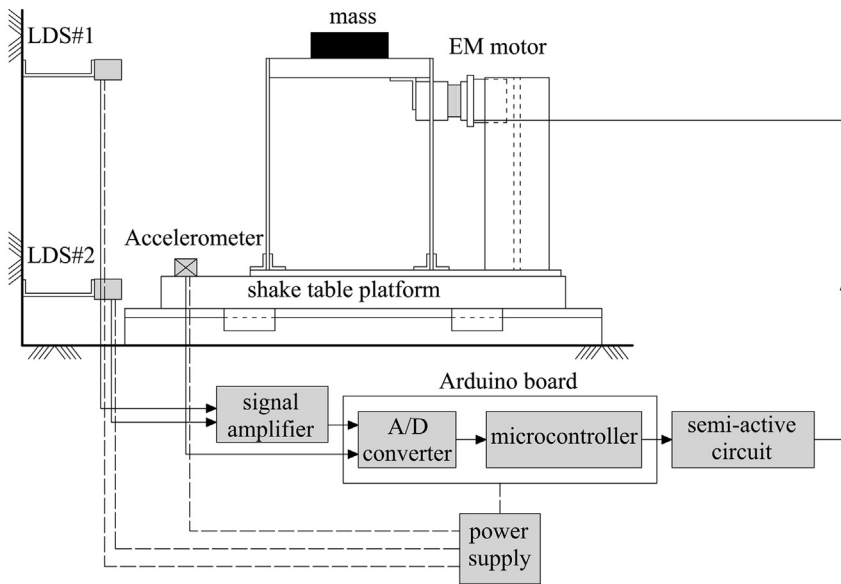


## (b) Semi-active mode



**Fig. 18.** Schematic diagram of the test set-up for (a) the passive energy harvesting mode and (b) the semi-active mode.
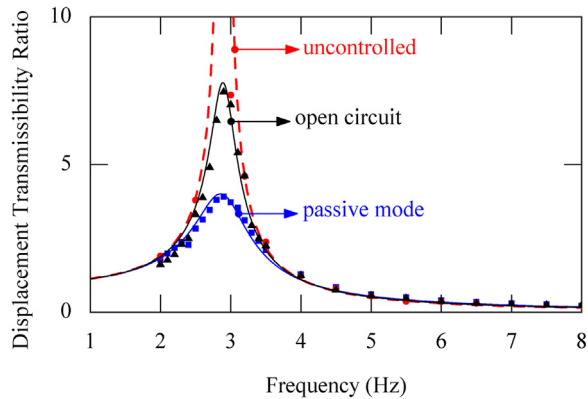


**Fig. 19.** Displacement transmissibility ratio (lines: theoretical, scattered points: experimental results).
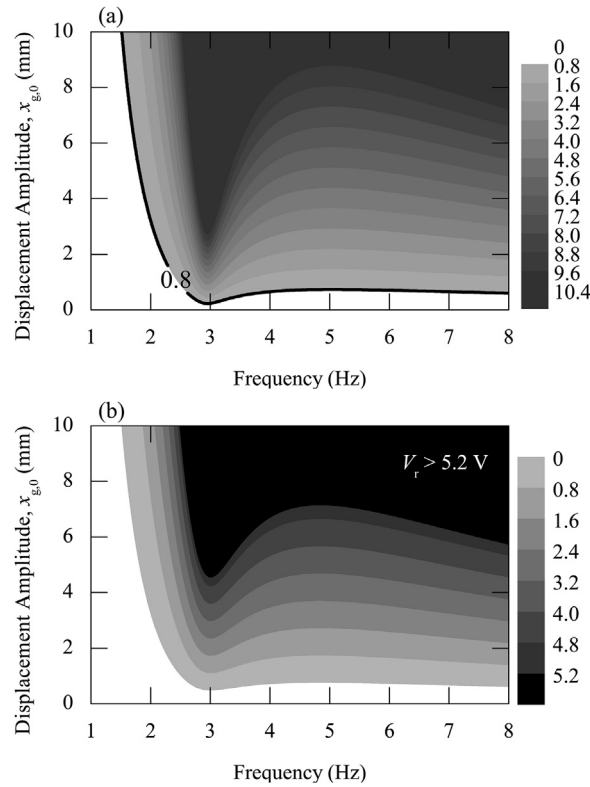
**Fig. 20.** (a) Open-circuit voltage amplitude $e_0$, (b) maximum rectifier voltage $V_r$.

$$e_0^{\text{passive}} = kx_{g,0}R_v\left(\omega;\omega_n,\xi_{\text{passive}}\right) \tag{38}$$

Fig. 20(b) shows the maximum rectifier voltage variation with respect to the base displacement and frequency. For the given duty cycle $D = 0.5$ and the rechargeable battery voltage $V_{\text{bat}} = 5.2$ V, the black region where $V_r > 5.2$ V represents the domain in which the DCM condition is no longer valid. Fig. 20(a) and (b) together define the operation region of the passive energy harvesting circuit.

In terms of the harvested energy, the efficiency of the damper defined in Eq. (14) is plotted in Fig. 21 when the model was excited with a 3-mm amplitude harmonic displacement. It is seen that no power is harvested for frequencies below 2 Hz. For the higher frequencies, the efficiency varies between 0.11 and 0.31, with an average value of 0.26.

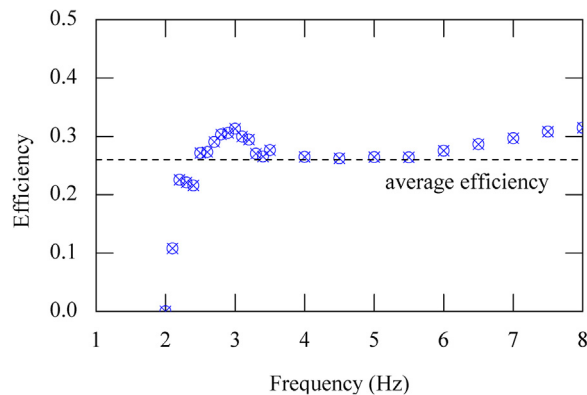The theoretical value for the harvested power can be approximated as,



**Fig. 21.** Total efficiency versus frequency.

$$\overline{P}_{\text{bat}} = \eta m \omega_n \xi_{\text{passive}} x_{g,0}^2 R_v^2 \left( \omega; \omega_n, \xi_{\text{passive}} \right) \tag{39}$$

In Fig. 22, the measured harvested power ($\overline{P}_{\text{bat}}$) is compared with the theoretical values calculated from Eq. (39).

### 6.3. Semi-active mode

Next, the semi-active circuit is connected to the terminals of the damper. The schematic diagram of the set-up and its components are shown in Fig. 18(b). In this experiment, two laser displacement sensors (LDS) are used to measure the displacements of the model and the shake table. The acceleration of the shake table is measured using an ADXL analog accelerometer. Since the control algorithm described in Section 5 is based on a full-state feedback control, both the displacement and velocity responses of the model are required to calculate the optimal input force. The velocity response is estimated from the measured displacements. Also, an exponential moving average (EMA) filter [35] is used to filter the sampled data in real time and attenuate the effect of the higher frequency noise.

The LQR control algorithm is used to construct the reference model for the SMC. The feedback gain matrix **G** (Eq. (22)) is found through the algebraic Riccati equation pertinent to the LQR control. The states weight matrix **Q** and the input weight $R$ are set as follows,

$$\mathbf{Q} = \begin{pmatrix} 2389 & 0 \\ 0 & 7.04 \end{pmatrix}, \quad R = 0.002 \tag{40}$$

For the sliding mode controller, the weighting factor vector is,

$$\mathbf{h} = \begin{bmatrix} 10 & 1 & 1 \end{bmatrix} \tag{41}$$

Based on the characterization of the damper, the bound of the parasitic force can be estimated to be around 2.5 N (Table 1). Hence, $\rho = 10$ is selected to ensure the sliding mode condition in Eq. (32) is satisfied.

A band-limited Gaussian noise with a range of 0–10 Hz and a variance of 2 mm is generated to excite the model. For the structural natural frequency of 2.93 Hz, this is an accurate estimation of a random white noise excitation. Fig. 23 shows the total displacement of the model for 30 seconds of excitation. It is seen that the semi-active EM damper with SMC can effectively moderate the displacement of the model. The root mean square (RMS) value of the displacement for the un-controlled case is 12.05 mm, and for SMC it is reduced to 3.35 mm.

In Fig. 24(a) and (b), the measured absolute acceleration and displacement of the SMC controller are compared with the corresponding responses calculated using the ideal LQR controller. In the ideal LQR case, the response of the structure is obtained for a linear system with no parasitic force. The small difference between the two cases demonstrates the success of SMC in tackling the effect of the nonlinear parasitic force, and how well it can track the response of the ideal LQR case.

It should be noted that for a structure under ground excitation, the added damping due to the parasitic force may have favorable effect on the relative displacement (drift) of the structure, but it can have negative impact on the absolute acceleration. This can affect the occupants comfort and be damaging to the building contents and non-structural components [36].
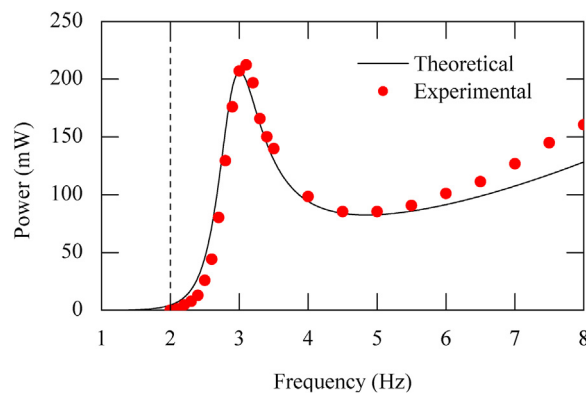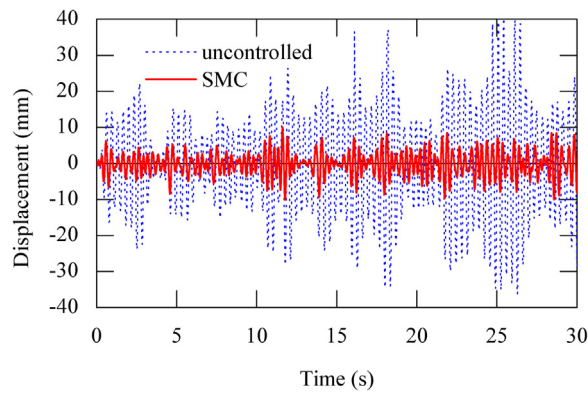


**Fig. 22.** Harvested power versus frequency.

**Fig. 23.** Comparison of displacements for the controlled and uncontrolled cases.
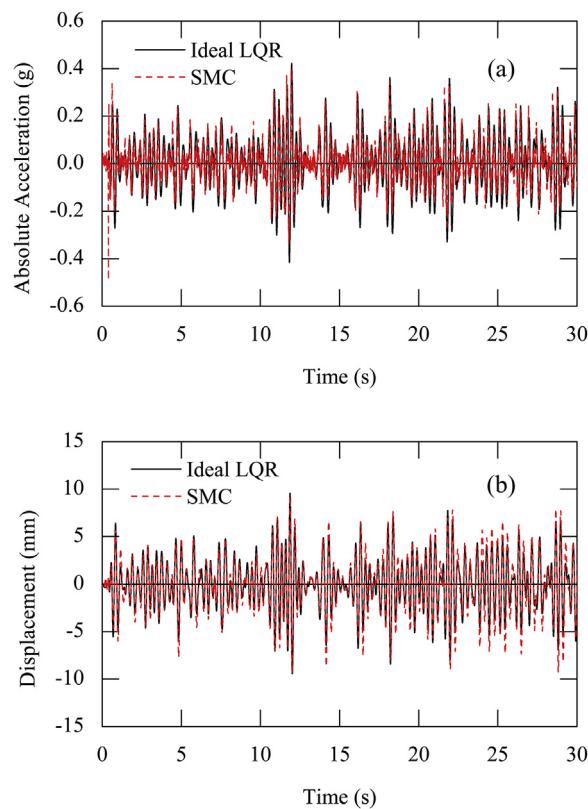


**Fig. 24.** Comparison of the sliding mode controller (SMC) with the ideal LQR case.

### 6.4. Comparison of the passive energy harvesting mode and the semi-active mode

In this section the performance of the two operational modes of the damper is compared with each other. For this purpose, the model is excited with a sine sweep ground displacement with an amplitude of 2 mm and the frequency range of 1.5−8 Hz. Fig. 25 illustrates the displacement response of the model for three cases, namely the open-circuit, the passive energy harvesting mode, and the semi-active mode. It is seen that the semi-active mode has the smallest displacement and apparently outperforms the other two cases. The passive harvesting mode also performs better than the open-circuit case. Fig. 26 illustrates the displacement frequency response functions of the model. In addition to the previous cases, the uncontrolled case is also added, in which the damper is completely removed from the structure. The comparison of the frequency domain responses across the considered frequency range reveals the advantage of the semi-active mode over the other cases. Particularly, it is evident that the displacement is significantly reduced around the resonant frequency.
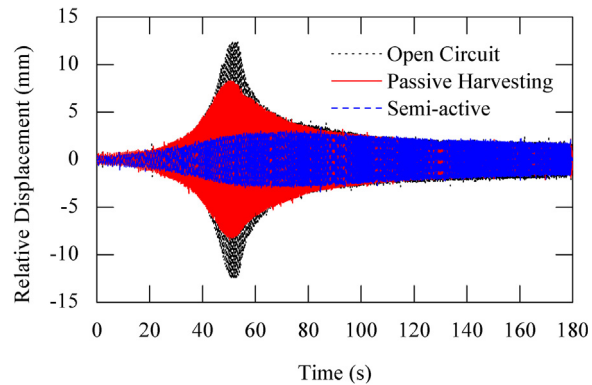
**Fig. 25.** Displacement time histories under sine sweep excitation (2 mm, 1.5–8.0 Hz).
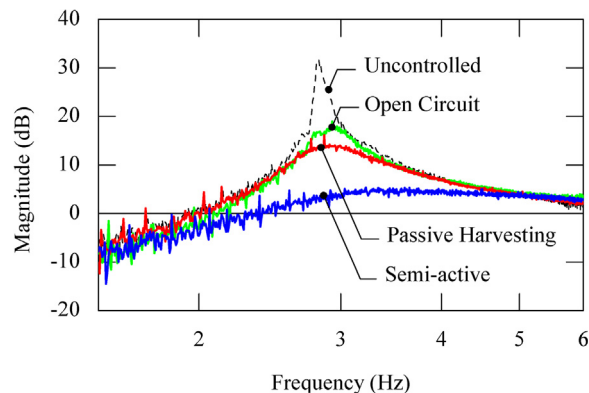


**Fig. 26.** Frequency response functions of the displacement.

## 7. Conclusions

Prototyping and experimental characterization were performed for a novel hybrid EM damper. This damper was designed to switch between a passive energy harvesting mode and a semi-active control mode depending on the amount of energy harvested and stored in the battery. Under harmonic excitation, the passive energy harvesting mode exhibited an actual average resistance close to the theoretical value. It is shown that the average efficiency of the passive energy harvesting mode is around 30%. In the semi-active case, a detailed explanation of the operation of the circuit was given, and the tuning range of the semi-active mode was experimentally verified. A sliding mode based controller was developed to address the effect of the nonlinear parasitic force appearing in addition to the electromagnetic force.

Finally, the prototype of the damper along with the control algorithm were examined in a laboratory setting, for vibration control of a small-scale shear frame structure. It is shown that the passive energy harvesting mode was able to increase the equivalent structural damping ratio of the model up to 6%. For the semi-active mode, the displacement response of the model under random band-limited Gaussian noise is presented. It is demonstrated that the sliding mode based controller could track the response of a closed-loop optimal system despite the effect of the nonlinear parasitic force. In order to have a full picture of the damper's performance, both modes were compared with the uncontrolled and open-circuit cases. Using a sine sweep excitation, the advantage of the semi-active mode over the other cases was displayed in terms of displacement mitigation.

Further studies are needed to investigate the full-scale application of the damper. To scale-up the damper, a larger EM motor with a larger motor constant is necessary. In that case, rotary motors might be more suitable options as they tend to have a smaller coil resistance and are able to generate a larger back-emf.

# References

[1] H.-J. Jung, I.-H. Kim, S.-J. Jang, An energy harvesting system using the wind-induced vibration of a stay cable for powering a wireless sensor node, Smart Mater. Struct. 20 (2011), 075001, https://doi.org/10.1088/0964-1726/20/7/075001.

[2] I.-H. Kim, S.-J. Jang, H.-J. Jung, Performance enhancement of a rotational energy harvester utilizing wind-induced vibration of an inclined stay cable, Smart Mater. Struct. 22 (2013), 075004, https://doi.org/10.1088/0964-1726/22/7/075004.

[3] S.P. Beeby, R.N. Torah, M.J. Tudor, P. Glynne-Jones, T. O'Donnell, C.R. Saha, S. Roy, A micro electromagnetic generator for vibration energy harvesting, J. Micromech. Microeng. 17 (2007) 1257–1265, https://doi.org/10.1088/0960-1317/17/7/007.

[4] S.P. Beeby, M.J. Tudor, N.M. White, Energy harvesting vibration sources for microsystems applications, Meas. Sci. Technol. 17 (2006) R175–R195, https://doi.org/10.1088/0957-0233/17/12/R01.

[5] L. Zuo, X. Tang, Large-scale vibration energy harvesting, J. Intell. Mater. Syst. Struct. 24 (2013) 1405–1430, https://doi.org/10.1177/1045389X13486707.

[6] S.J. Elliott, M. Zilletti, Scaling of electromagnetic transducers for shunt damping and energy harvesting, J. Sound Vib. 333 (2014) 2185–2195, https://doi.org/10.1016/j.jsv.2013.11.036.

[7] L. Zuo, W. Cui, Dual-functional energy-harvesting and vibration control: electromagnetic resonant shunt series tuned mass dampers, J. Vib. Acoust. 135 (2013), 051018, https://doi.org/10.1115/1.4024095.

[8] X. Tang, L. Zuo, Simultaneous energy harvesting and vibration control of structures with tuned mass dampers, J. Intell. Mater. Syst. Struct. 23 (2012) 2117–2127, https://doi.org/10.1177/1045389X12462644.

[9] K. Takeya, E. Sasaki, Y. Kobayashi, Design and parametric study on energy harvesting from bridge vibration using tuned dual-mass damper systems, J. Sound Vib. 361 (2016) 50–65, https://doi.org/10.1016/j.jsv.2015.10.002.

[10] W. Shen, S. Zhu, Y. Xu, An experimental study on self-powered vibration control and monitoring system using electromagnetic TMD and wireless sensors, Sens. Actuators Phys. 180 (2012) 166–176, https://doi.org/10.1016/j.sna.2012.04.011.

[11] A. Gonzalez-Buelga, L.R. Clare, A. Cammarano, S.A. Neild, S.G. Burrow, D.J. Inman, An optimised tuned mass damper/harvester device, Struct. Control Health Monit. 21 (2014) 1154–1169, https://doi.org/10.1002/stc.1639.

[12] S. Zhu, W. Shen, Y. Xu, Linear electromagnetic devices for vibration damping and energy harvesting: modeling and testing, Eng. Struct. 34 (2012) 198–212, https://doi.org/10.1016/j.engstruct.2011.09.024.

[13] W. Shen, S. Zhu, Harvesting energy via electromagnetic damper: application to bridge stay cables, J. Intell. Mater. Syst. Struct. 26 (2015) 3–19, https://doi.org/10.1177/1045389X13519003.

[14] R. Palomera-Arias, J.J. Connor, J.A. Ochsendorf, Feasibility study of passive electromagnetic damping systems, J. Struct. Eng. 134 (2008) 164–170, https://doi.org/10.1061/(ASCE)0733-9445(2008)134:1(164).

[15] D. Niederberger, S. Behrens, A.J. Fleming, S.O.R. Moheimani, M. Morari, Adaptive electromagnetic shunt damping, IEEE ASME Trans. Mechatron. 11 (2006) 103–108, https://doi.org/10.1109/TMECH.2005.859844.

[16] S. Takeuchi, K. Makihara, J. Onoda, Reliable and evolvable vibration suppression by self-powered digital vibration control, J. Vib. Acoust. 134 (2012), 024502, https://doi.org/10.1115/1.4005027.

[17] B. Sapiński, Energy-harvesting linear MR damper: prototyping and testing, Smart Mater. Struct. 23 (2014), 035021.

[18] J. Gołdasz, B. Sapiński, Energy harvesting MR dampers, in: Insight Magnetorheol. Shock Absorbers, Springer International Publishing, Cham, 2015, pp. 173–201, https://doi.org/10.1007/978-3-319-13233-4_9.

[19] C. Chen, W.-H. Liao, A self-sensing magnetorheological damper with power generation, Smart Mater. Struct. 21 (2012), 025014, https://doi.org/10.1088/0964-1726/21/2/025014.

[20] M. Jamshidi, C.C. Chang, A. Bakhshi, Self-powered hybrid electromagnetic damper for cable vibration mitigation, Smart Struct. Syst. 20 (2017) 285–301, https://doi.org/10.12989/sss.2017.20.3.285.

[21] G. Lesieutre, G. Ottman, H. Hofmann, Damping as a result of piezoelectric energy harvesting, J. Sound Vib. 269 (2004) 991–1001, https://doi.org/10.1016/S0022-460X(03)00210-4.

[22] G.K. Ottman, H.F. Hofmann, G.A. Lesieutre, Optimized piezoelectric energy harvesting circuit using step-down converter in discontinuous conduction mode, IEEE Trans. Power Electron. 18 (2003) 696–703, https://doi.org/10.1109/TPEL.2003.809379.

[23] G.K. Ottman, H.F. Hofmann, A.C. Bhatt, G.A. Lesieutre, Adaptive piezoelectric energy harvesting circuit for wireless remote power supply, IEEE Trans. Power Electron. 17 (2002) 669–676, https://doi.org/10.1109/TPEL.2002.802194.

[24] E. Lefeuvre, D. Audigier, C. Richard, D. Guyomar, Buck-boost converter for sensorless power optimization of piezoelectric energy harvester, IEEE Trans. Power Electron. 22 (2007) 2018–2025, https://doi.org/10.1109/TPEL.2007.904230.

[25] E. Lefeuvre, A. Badel, C. Richard, D. Guyomar, Piezoelectric energy harvesting device optimization by synchronous electric charge extraction, J. Intell. Mater. Syst. Struct. 16 (2005) 865–876, https://doi.org/10.1177/1045389X05056859.

[26] Linear Voice Coil Motors, Moticont, 2017. http://www.moticont.com/voice-coil-motor.htm. (Accessed 10 October 2017).

[27] Arduino, (2017). https://www.arduino.cc/(Accessed October 10, 2017).

[28] I.L. Cassidy, J.T. Scruggs, S. Behrens, H.P. Gavin, Design and experimental characterization of an electromagnetic transducer for large-scale vibratory energy harvesting applications, J. Intell. Mater. Syst. Struct. 22 (2011) 2009–2024, https://doi.org/10.1177/1045389X11421824.

[29] P.L. Green, K. Worden, N.D. Sims, On the identification and modelling of friction in a randomly excited energy harvester, J. Sound Vib. 332 (2013) 4696–4708, https://doi.org/10.1016/j.jsv.2013.04.024.

[30] D.W. Marquardt, An algorithm for least-squares estimation of nonlinear parameters, J. Soc. Ind. Appl. Math. 11 (1963) 431–441.

[31] N.G. Stephen, On energy harvesting from ambient vibration, J. Sound Vib. 293 (2006) 409–425, https://doi.org/10.1016/j.jsv.2005.10.003.

[32] M. Yokoyama, J.K. Hedrick, S. Toyama, A model following sliding mode controller for semi-active suspension systems with MR dampers, in: IEEE, vol. 4, 2001, pp. 2652–2657, https://doi.org/10.1109/ACC.2001.946276.

[33] L.M. Jansen, S.J. Dyke, Semiactive control strategies for MR dampers: comparative study, J. Eng. Mech. 126 (2000) 795–803, https://doi.org/10.1061/(ASCE)0733-9399(2000)126:8(795).

[34] H.K. Khalil, Nonlinear Systems, third ed., Prentice Hall, Upper Saddle River, N.J, 2002.

[35] R.G. Lyons, Understanding Digital Signal Processing, first ed., Addison-Wesley Longman Publishing Co., Boston, MA, USA, 1996.

[36] E. Miranda, S. Taghavi, Approximate floor acceleration demands in multistory buildings. I: formulation, J. Struct. Eng. 131 (2005) 203–211, https://doi.org/10.1061/(ASCE)0733-9445(2005)131:2(203).